Materials Advances

ROYAL SOCIETY OF CHEMISTRY

PAPER

View Article Online
View Journal | View Issue

Cite this: *Mater. Adv.*, 2025, 6, 3665

Plasmonically optimized gold–gallia nanocomposites: a novel approach for high-temperature NO_2 detection†

L. Keerthana,[a] Mushtaq Ahmad Dar,[b] R. Sivasubramanian [c] and Gnanaprakash Dharmalingam *[a]

Received 18th February 2025,
Accepted 18th April 2025

DOI: 10.1039/d5ma00151j

rsc.li/materials-advances

Monitoring gases in harsh environments in real-time has become indispensable across various industries such as nuclear plants, turbines, and boiler plants. Materials capable of withstanding high temperatures are essential for sensing platforms, often operating at temperatures exceeding 300 °C. Localized surface plasmon resonance based optical gas sensing, although promising, has a glaring limitation when sensing analytes that themselves interact with light in wavelength regimes that overlap with the material's resonance, which is remedied in one manner in this report. In this study, we synthesize multiple gold–gallium oxide nanocomposites that were evaluated for their morphological and optical stabilities at high temperatures (800 °C), post which they were tested for NO_2 detection at 800 °C, wherein temperature-dependent kinetic studies were conducted first to deconvolute the absorbance of NO_2 itself at different temperatures. The findings suggest that gold–gallium oxide nanocomposites prepared using the described solution-based approach show promising applications in high-temperature and extreme environment gas sensing.

1. Introduction

Over the years, urbanization and industrialization have led to a rise in the prevalence of pollution from various sources, resulting in environmental degradation.[1] High-temperature combustion sources produce pollutants like NO_2, such as boiler plants (500–700 °C), gas turbines (>800 °C), steam turbines (400–600 °C), and glass-making industries (400–700 °C), in the concentration ranges 250–650 ppm, 2–20 ppm, 141–929 ppm, and 640 ppm, respectively.[2] NO_2 is one of the main contributors to the formation of tropospheric ozone and acid rain, affecting the quality of soil and water and human health, causing respiratory problems, nausea, dizziness, *etc.*[3] Usually, real-time data pertaining to NO_2 emissions from combustion sources are unavailable. To increase the accuracy of NO_2 quantification from these sources, it is important to have sensors with materials that can operate reliably, even at elevated temperatures. Optical sensors have attributes such as non-contact detection, flexibility in monitoring multiple parameters (peak intensity, centroid, and peak position), high sensitivity,[4] and being amenable to miniaturization through the use of narrow wavelength optics such as diodes and photodetectors, where for example generic solid-state semiconductors suffer from degradation of electrical contacts (when at temperatures >500 °C typically) though being cost-effective.[5] Thus a suitable approach is proposed to employ plasmonic materials incorporated in metal oxides for high-temperature (800 °C) detection of NO_2. Indeed, such an approach has already been reported by us and others. Among the plasmonic metals (Cu, Ag, Au, Pt, Pd, *etc.*), Au nanoparticles (AuNPs) are potential candidates owing to their high-temperature compositional stability and intricate tunability of the plasmon peak to achieve maximum sensitivity and being a good catalyst for multiple reactions,[6–8] with sensitivity corresponding to the quantified changes in a material's observed property (the plasmon peak for plasmonic optical sensing applications, for example). Integrating AuNPs with metal oxides like TiO_2, SiO_2, ZrO_2, *etc.* promotes thermal stability and creates oxygen vacancies for enhancing materials' sensitivity.[9–15] In this work, Ga_2O_3 has been integrated as a matrix with AuNPs due to its high thermal stability (1100 °C), transparency in the visible region, and wide band gap (4.8 eV).[16] Wide band gap materials allow for higher operating temperatures and better thermal conductivity since they have a relatively ordered crystal structure, which allows for more efficient phonon transport and hence a higher thermal conductivity.[17–19] They also have higher phonon frequencies,

[a] *Plasmonic Nanomaterials Laboratory, PSG Institute of Advanced Studies, Coimbatore-641004, India. E-mail: dgp@psgias.ac.in*
[b] *Center of Excellence for Research in Engineering Materials, Deanship of Scientific Research (DSR), King Saud University, Riyadh 11421, Saudi Arabia*
[c] *Department of Chemistry, Amrita School of Engineeering, Amrita Vishwa Vidyapeetham, Amaravati, Andhra Pradesh, India*

† Electronic supplementary information (ESI) available. See DOI: https://doi.org/10.1039/d5ma00151j

which result in shorter mean free paths, carrying heat more effectively, thus making them resistant to higher temperatures.[20] Thus these factors are crucial in high temperature sensing where precise control of material parameters is desired over long durations.[21] Our group and others have fabricated such AuNP–metal oxide composites through physical vapor deposition, lithography, chemical vapor deposition *etc.*, which make use of power intensive and expensive equipment.[22–24] Here, we have explored a solution-based approach for synthesizing the same, wherein composites of Au and Ga_2O_3 (AGO) have been synthesized using two approaches *viz.*, (i) AuNPs of different morphologies (nanospheres and nanorods) integrated with gallium oxide through a hydrothermal process and (ii) defined morphologies of Ga_2O_3 incorporated with Au nanospheres through a hydrothermal approach. The synthesized AGOs have been tested for their thermal stability and NO_2 detection at 800 °C through a surface plasmon-based approach for the first time. Our group has already demonstrated that one of the AGOs is sensitive to concentration changes of CO at 800 °C and is morphologically and compositionally stable for at least 200 h of CO exposure at this temperature.[25] Detecting NO_2 through optical approaches has an inherent problem, in that NO_2 itself absorbs in the visible range. Hence, a change in any optical metric (which is the scrutiny that is done to confirm a sensing response) cannot be only due to a change in the sample's optical properties and will be a convolution of the sample and the gas absorption changes. We present here a simple solution of measuring a baseline response with only NO_2 wherein the degree of change in absorbance for wavelengths overlapping with the samples' absorption is first quantified. After this, a similar measurement is done with the sample being exposed to NO_2. By confirming the change in the degree of absorbance between the two, we confirm the presence of a distinct response of the sample to NO_2. In addition to quantifying the sensing response, we have investigated the kinetics of the sensing mechanism substantiated by theory, experiments, and previous findings. We demonstrate thus that AGOs synthesized using simple solution-based approaches exhibit a multitude of hours of thermal stability, are responsive to NO_2 at 800 °C, and can be utilized as potential candidates for real-time monitoring of such gases of concern in combustion environments.

2. Materials and methods

2.1 Synthesis of AGO

The details of the synthesis of AuNPs, as well as defined morphologies of Ga_2O_3 such as hexagonal plates and nanorods, have been reported elsewhere.[26,27] Briefly, AuNPs of various morphologies such as spheres, rods and flowers were synthesized using different reducing agents through irradiation with microwaves at a power of 425 W for 4 min. Similarly, Ga_2O_3 morphologies were synthesized using CTAB as a growth directing agent and microwave irradiation at a power of 425 W for 4 minutes.

Two groups of AGOs have been investigated in this work. For the first group, AuNPs synthesized through a microwave method (resulting in spheres with average diameters of 5 nm and 25 nm and the samples are designated as 5S and 25S) and through chemical reduction (resulting in nanorods with average aspect ratios of 2R, 3R, and 4R) were incorporated into 10 mL of a 1 mM aqueous solution of gallium nitrate ($GaNO_3$, Sigma Aldrich 99.9%) and placed in a hydrothermal reactor, where they were subsequently heated at 180 °C for 16 h. For the second group, defined gallium oxide morphologies (rods and hexagonal plates) as well as undefined Ga_2O_3 (prepared through a hydrothermal process) were synthesized using a combination of the microwave method and hydrothermal method, each of which was then added separately into separate 10 mL solutions of an aqueous solution containing 25S, transferred to a hydrothermal reactor, and subjected to heating at 180 °C for 16 h. Following this, the solutions obtained through both approaches were washed multiple times with water and centrifuged at 10 000 rpm. Table 1 lists all the samples that have been investigated in this work and the nomenclatures that have been used for them. Group I comprises samples that involve different morphologies of Au NPs, which were combined with Ga_2O_3 through a hydrothermal approach, and group II comprises samples wherein defined as well as randomly formed morphologies of Ga_2O_3 were used to form composites with the same Au NPs' morphology of spheres with an average diameter of 25 nm.

The AGOs were dispersed in isopropyl alcohol (IPA) and deposited onto quartz substrates at an optimized rotational speed of 1500 rpm to achieve maximum absorbance. Later, they were dried at 90 °C and finally subjected to annealing at 850 °C. A schematic representation of the synthesis of the two groups of plasmonic composites is shown in Fig. 1.

2.2 Gas sensing and data analysis

Sensing experiments involved monitoring the optical absorbances of both NO_2 and the samples between the wavelength range of 350 nm and 1000 nm using a Flame-T-visible-NIR

Table 1 List of AGOs synthesized using different approaches *viz.*, group I and group II

Group	Composite composition	Sample ID	Proportions of AuNPs/Ga_2O_3 taken to form the composites
Group-I	5S + $GaNO_3$	5SC	10 mL of AuNPs + 10 mL of 1 mM $GaNO_3$
	2R + $GaNO_3$	2RC	
	3R + $GaNO_3$	3RC	
	4R + $GaNO_3$	4RC	
Group-II	25S + $GaNO_3$	AIGO	
	25S + HGO	AHGO	10 mL of 25S + 10 mg of Ga_2O_3 morphologies
	25S + GOR	AGOR	
	25S + GOH	AGOH	
	25S + CGO	ACGO	

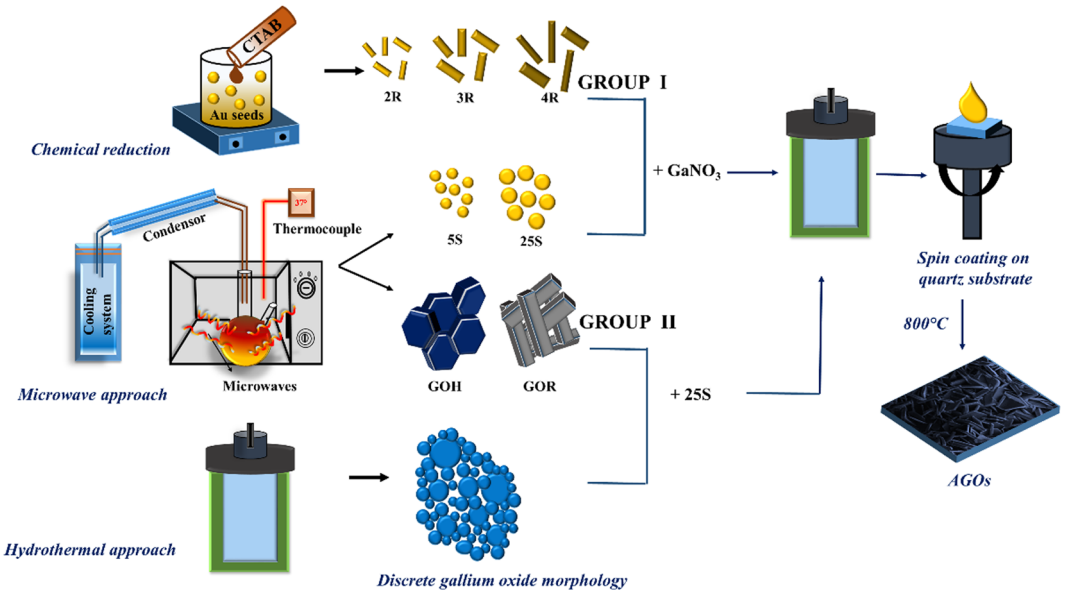

Fig. 1 Fabrication protocols of the different investigated AGOs.

spectrometer from Ocean Optics. AGOs spun on quartz substrates were placed inside a horizontal split-type tubular furnace (Indfurr Superheat Furnaces, India), with provisions for flowing different concentrations of air as well as NO_2 using Alicat Scientific mass flow controllers (MFCs). The percentage of NO_2 present in the cylinder was 1% (air balance). Compressed air at appropriate flow rates was used as the background/carrier gas. The complete setup is shown in Fig. 2, wherein an absorbance measurement is made with air as the reference. The first tests were on the changes in absorbance detected by the spectrometer when only NO_2 was flowed into the chamber at 800 °C. Multiple exposures were done at each concentration of 500 ppm, 1000 ppm, 2500 ppm, and 5000 ppm in order to get the average change in absorbance, presented in Section 3.5. The concentration of the gas (in ppm) was calculated based on the ratio between the gas flow (in SLPM) of the target gas (NO_2) and that of the carrier gas (air). Flow vision software was used to program and control the gas flow. Post these trials and prior to the sensing tests, the composites were tested for their thermal stability (TS) *i.e.* their ability to withstand without degradation the temperature of 800 °C wherein they were heated to 800 °C at a ramp rate of 10 °C min^{-1} with continuous purging of air at a flow rate of 2 standard litres per minute (SLPM). Absorption spectra were collected every 5 s from room temperature to 800 °C

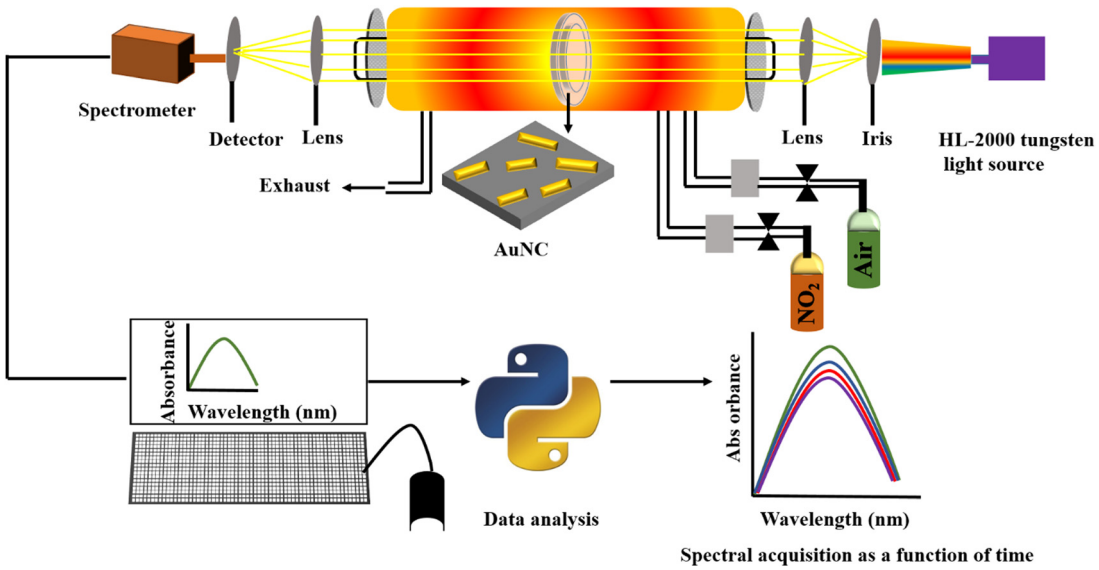

Fig. 2 Setup for optical sensing of NO_2 at elevated temperatures, with mass flow controllers for regulating NO_2 concentrations, a horizontal split-type furnace designed for optical measurements of samples in a ceramic holder, and optical elements such as collimators, plano-convex lenses, a light source, and a spectrometer.

and for 2 h (the typical duration of a TS study) at this temperature. The results of the TS studies have been reported elsewhere.[28] Briefly, these studies revealed that AGOs 2RC and 3RC underwent a structural transformation (from rods to spheres, evident from the disappearance of the longitudinal plasmon band), whereas all other AGOs were found to be morphologically more stable at 800 °C for the tested duration of two hours. Even though 2RC and 3RC had undergone structural transformation, the resulting spherical particles were stable against further changes, as the plasmon bands were unvarying at 800 °C post this change. Hence, all the AGOs were tested to detect NO_2.

After the TS tests and ascertaining the suitability of these composites for high temperature sensing, they were exposed to NO_2 at 800 °C. During the sensing experiments the sample was initially heated to 800 °C at a rate of 10 °C min^{-1}, and this temperature was sustained for 1 h while a continuous airflow was maintained at a flow rate of 2 SLPM. Post this step NO_2 was flowed into the setup with the aforementioned concentrations, wherein the NO_2 stream coming from a separate mass flow controller was mixed with the already flowing stream of the carrier gas before entry into the sensing chamber. The initial purging with air allowed the sample to stabilize its response to O_2 (present in the carrier air) at the temperature before NO_2 was introduced, allowing confirmation to be made that any change to the absorbance spectra when the NO_2/air mixture was flowed into the sensing chamber was due to reactions with NO_2. Measurements of the changes to the absorbance intensities during these exposures were then performed using an in-house Python script and are discussed in Section 3.

2.3 Characterization techniques

UV-visible absorption spectra were obtained using a Flame-T-visible spectrometer (Ocean Optics). The crystalline structure of AGO was examined *via* X-ray diffraction (XRD) with an Empyrean device from Malvern Panalytical, utilising Cu-Kα radiation (λ = 1.54 Å). The diffractograms were recorded within a 2θ range of 20° and 90°. Morphological characteristics of the synthesized nanocomposites were analysed using transmission electron microscopy (TEM) images and energy dispersive X-ray spectra (EDS) with a JOEL JEM 2100 at an accelerating voltage of 200 kV. For TEM, colloidal suspensions were coated on copper grids and dried at room temperature. The surface morphology and elemental analyses were done using a ZEISS EVO 18 scanning electron microscope (SEM) operating at an accelerating voltage of 20 kV.

3. Results and discussion

This section discusses the following topics, *viz.*, results of optical absorbance investigations of the composites and TS tests (Section 3.1), the diffraction studies on the AGOs (Section 3.2), the morphological characterization (Section 3.3), and the scrutinization of the NO_2 responses of the AGOs at 800 °C (Section 3.4).

3.1 Optical absorbance investigations of the composites and TS studies

Optical studies have been carried out to analyze the absorbance of the synthesized AGOs and their corresponding thermal stability to confirm the presence of AuNPs in the composites. The synthesized AGOs exhibit their characteristic peaks in the region of 500–650 nm (in the case of spheres) due to the collective oscillation of conduction electrons in the AuNPs termed as localized surface plasmon resonance, and interband transitions are entrenched reasons for this absorption.[29] These AGOs were tested for their thermal stability prior to gas sensing tests to evaluate their stability after exposure to 800 °C for 2 h. Upon integration of pristine Au nanostructures (AuNSs and AuNRs), with Ga_2O_3 using a hydrothermal process, AuNRs underwent a morphological transformation (rods to spheres) due to high-temperature exposure confirmed by the optical absorbance studies (monitored *in situ*) for all the composites, which showed a shift in the plasmon peak as well as the change of two distinct peaks into one. AuNRs tend to undergo thermal reshaping *via* surface diffusion as temperature increases, evolving towards a lower aspect ratio (*i.e.*, a spherical shape). Kennedy *et al.* have studied this reshaping dynamics at elevated temperatures for example and reported that the AuNRs undergo shape transformations and that this behaviour was consistent across all the aspect ratios.[30]

Unlike AuNRs, composites (2RC and 3RC) and AuNSs (5SC and group II AGOs) were found to be relatively more stable against changes to morphology, as post TS tests all AGOs exhibited the presence of the characteristic plasmon peak of AuNPs, albeit with varying degrees of shift in this peak towards longer wavelengths *i.e.*, a redshift (to varying degrees between 2 nm and 10 nm) due to an increase in AuNP volume at high temperature.[30] A representative absorbance graph as well as the TS graph of the best responding AGO (to NO_2, *i.e.*, AIGO, the reasons for which will be discussed in the subsequent sections) is presented in the ESI† as Fig. S1 and S2 respectively.

As shown in Fig. 3, following the TS tests, a 4 nm red shift has been noted, attributable to Ostwald ripening and/or aggregation characterized by the growth of larger particles at the expense of smaller ones and/or the clustering of particles, respectively, in addition to alterations in surface structure including changes in

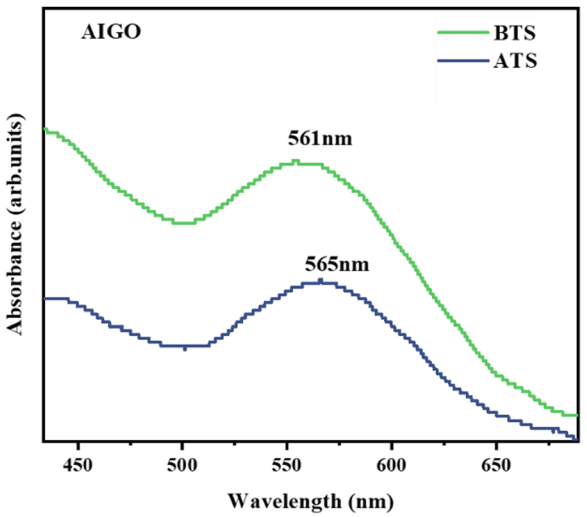

Fig. 3 Optical absorbance of the AIGO composite recorded before and after TS tests at room temperature. Reproduced with permission from ref. 30.

the type and concentration of roughness features/surface sites *etc.*[31,32] These conclusions have been arrived at from the fact that a redshift in the plasmon wavelength post exposure to only temperature, without any changes in material compositions and the surrounding dielectric, is indicative of an increase in the average nanoparticle volume, and that the phenomena of ripening and/or agglomeration at high temperatures have been well-established. Although direct visualization of the samples would have confirmed these conclusions, limitations of the characterization techniques used (SEM and TEM) preclude imaging since the nanoparticles incorporated are below 50 nm (precluding SEM imaging) and are dispersed on a 1 mm thick quartz substrate (precluding TEM). Hence the confirmations regarding particle morphology changes have been arrived at from the optical absorbance changes, which have been valuable to judge the same, as confirmed through this report and others.

3.2 Diffraction studies on the AGO composites

Diffraction studies have been performed to confirm the presence of Au and Ga_2O_3 before and after TS tests. The diffraction patterns exhibit the Bragg reflection planes (111), (110), (220), and (311) of Au for all the AGOs, whereas the reflection planes of Ga_2O_3 differ owing to formation of different phases such as β and γ. Among the polymorphs of Ga_2O_3, the β phase has high thermal and phase stability up to 1100 °C, which has been confirmed through thermal stability tests.[33] All the reflection planes corresponding to the β phase have been observed except for the γ phase, which showed maximum lattice distortions. Since the lattice distortions are temperature-driven parameters wherein the atoms tend to shift from their equilibrium position by gaining kinetic energy and influence the stability and phase composition, they play a crucial role in tailoring the light–matter interactions and optical properties, which directly influence the sensing performance of the composites.[34] Thus, to confirm the lattice distortions in the unit cell (after TS tests), Rietveld refinement (using Xpert HighScore software) has been performed for the AGOs comprising distinctive and discrete morphologies (AIGO, AGOH, AGOR, ACGO, and AHGO). From the analysis, it was confirmed that the AGOH exhibited maximum distortion compared to the pristine Ga_2O_3, whereas the AIGO had minimum distortion. Furthermore, statistical parameters derived from the reliable factors (*R*-value) confirm that AIGO had a lower goodness of fit (3.66) value compared to other AGOs due to minimum distortion in the crystal lattice. Since all the other AGOs (5SC, 2RC, 3RC, and 4RC) have been integrated through an *in situ* method similar to AIGO, these AGOs have been exempted from the analysis as they possess only the pure phase of β-Ga_2O_3. We observe a decrease in the crystallite sizes corresponding to the dominant (111) plane for all AGOs, which is envisaged as due to the high-temperature exposure (800 °C) tending to increase the crystallinity, which subsequently decreases the grain size.[28,30] Also, no other peaks corresponding to crystalline/amorphous phases confirm the absence of contaminants in the samples. The diffraction patterns of the AGOs, Rietveld parameters, and the crystallite size corresponding to the (111) plane of Au are given in the ESI† (Fig. S3–S6). Diffraction patterns of AIGO before and after TS tests are presented in Fig. 4.

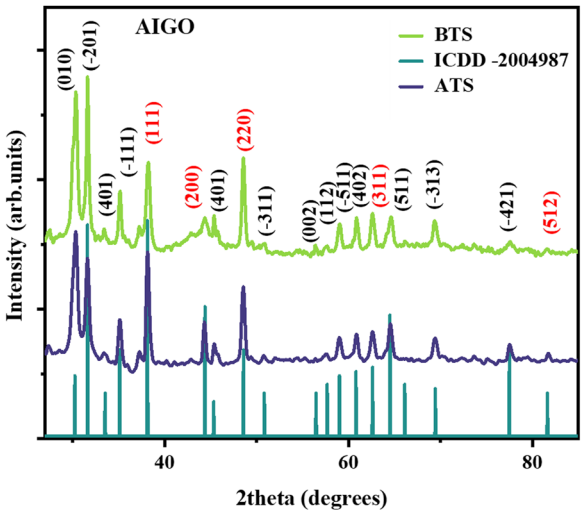

Fig. 4 Diffraction patterns of AIGO before and after TS tests. Reproduced with permission from ref. 27.

Based on the XRD analysis in Fig. 4, the peaks of Au have been retained. The % change in the crystallite size has been determined for the (111) plane of Au and is presented in the ESI† as Fig. S6.

3.3 Morphological characterization of the AGO composites

Morphologies of the AuNPs and Ga_2O_3 are important to achieve the tunable absorption desirable for gas sensing applications. The surface morphology of Ga_2O_3, as well as AuNP structures (spheres and rods), prepared through a microwave approach and their growth mechanisms have been studied by our group methodically.[33] AGOs prepared using the hydrothermal approach have been subjected to morphological analysis to understand the dimensions and the interaction between the host and support matrix (Au–Ga_2O_3). SEM analyses were performed for AGOR, AGOH, and ACGO composites, and their elemental compositions were further confirmed using EDS. TEM analysis has been performed for other composites such as AIGO and ACGO, which confirmed the presence of discrete morphologies of Ga_2O_3 with the uniform dispersion of AuNPs. The SEM images and their corresponding EDS graphs, TEM images, and dimensions of all the composites obtained through SEM analysis using ImageJ software are given in Fig. S7 and S8 (ESI†), respectively. The TEM image and SAED pattern of the representative AIGO composite are presented in Fig. 5.

3.4 NO_2 sensing investigations on AGOs

Post a detailed morphological and structural analysis, we have investigated the response of the different sample architectures to NO_2. Accordingly, this section has been divided into the determination of the changes in absorbance observed when only NO_2 was present in the sensing chamber (*i.e.* without any sample), in Section 3.4.1, the changes in absorbance observed when the different samples were exposed to the same concentrations of

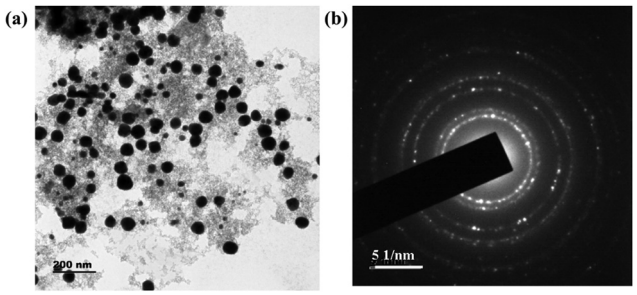

Fig. 5 (a) TEM images of the AIGO composite depicting the presence of Au and Ga_2O_3. (b) SAED diffraction pattern of AIGO with ring patterns and bright spots confirming the crystallinity of the composite. Reproduced with permission from ref. 28 and 30.

NO_2 (as in Section 3.4.1), as revealed in Section 3.4.2, the reaction mechanisms between the sample and NO_2 as elaborated in 3.4.3, and finally examination of temperature driven kinetics as detailed in Section 3.4.4.

3.4.1 Scrutinization of the absorbance of NO_2 gas in the visible region. Since NO_2 inherently absorbs in the visible region, deconvoluting changes in absorbance as being due to the samples' response and not due to NO_2 itself poses a serious issue.[35] An in-depth analysis has initially been carried out to understand the underpinning mechanism of the absorbance of NO_2 in the visible region to understand light–gas molecule interactions as influencers of sensing. From Fig. 6(a) it is observed that the absorbance intensity of NO_2 has gradually increased between the wavelength range of 450 nm and 600 nm with respect to temperature. NO_2 being a polar molecule has a lone pair of electrons on the nitrogen, and any entity in possession of either a non-bonding electron or π-bonds is highly susceptible to transitions that occur in the visible region.[36] The broad absorption reflects multiple wavelengths of light promoting electrons (non-bonding electrons or π-bonds) from discrete bonding to anti/non-bonding orbitals.[37,38]

NO_2 absorbance is extensively overlapped by that of its dimer N_2O_4 at any temperature and pressure. Experiments were carried out under conditions where N_2O_4 would not exist (since it absorbs below 400 nm and the acquisitions are not done at this wavelength), revealing that the absorbance of NO_2 was at 420 nm.[39] Another study reports that the absorbance of N_2O_4 alone was at 240 nm, wherein to minimize the absorbance of the dimer, measurements were performed at low pressures. A study analyzed the temperature dependent absorbance of NO_2 and N_2O_4 in the temperature range of 213–298 K and between 310 and 570 nm using a diode array spectrometer wherein spectral changes were recorded with an increase in temperature in this region of interest. The changes in the absorbance spectral profile were observed with respect to temperature, whereas no such temperature effects were reported for N_2O_4.[40] A tangible absorption cross-section of NO_2 in the range of 300–500 nm, with that of N_2O_4 occurring below 400 nm, has also been reported.[41]

With this understanding of the contributions to the observed absorbance profile, the absorbance profile of N_2O_4 can be overlooked since the wavelength monitored is in the range of 400–1100 nm. It is to be noted that upon increasing the temperature, the equilibrium toward producing more NO_2 gas molecules is likely,[34] a result of which could be seen from the testing chamber changing to dark brown. Upon cooling, the equilibrium shifts backward towards N_2O_4 production. It is important to note that to date, there have been only two reports on the examination of absorbance of N_2O_4, at the wavelengths of 190 nm and 210 nm.[34,41]

From Fig. 6(b) it is clear that the optical absorbance of the gas molecules overlaps with the plasmonic band of the AIGO, which makes the deconvolution of the sensor response uncertain. In plasmonic sensing, apart from the commonly used parameter retrieving the response towards an analyte by monitoring the centroid/peak position, the intensity as a function of time/temperature/wavelength can also be monitored. The centroid/peak position monitoring has the benefit of offering a good signal-to-noise ratio (S/N) when used with techniques such as the polynomial fit function that works on the least squares principle.[42] In our work, since the plasmon peak

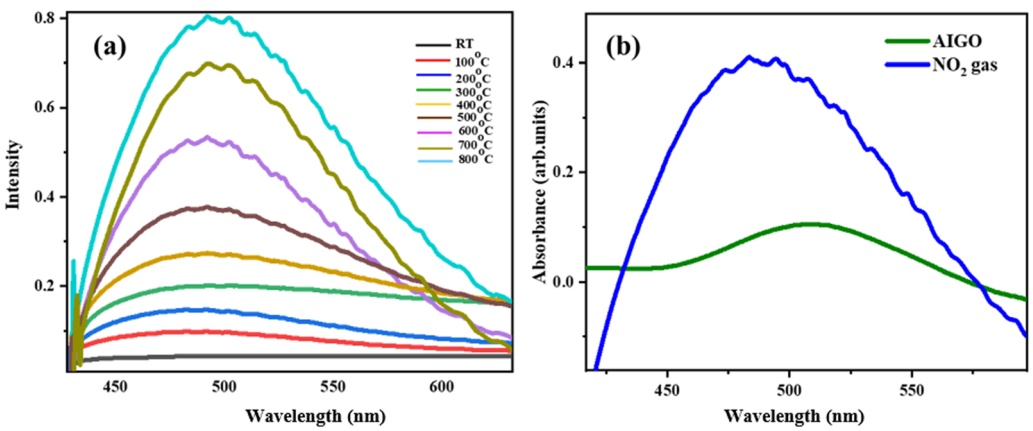

Fig. 6 (a) Absorbance of NO_2 gas as a function of temperature in the wavelength range of 450–600 nm and (b) superimposed optical absorbance of AIGO and NO_2 gas.

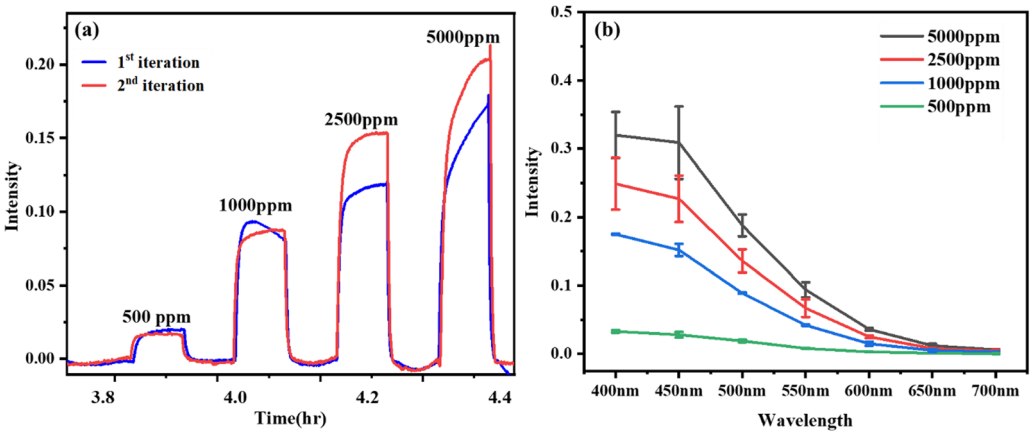

Fig. 7 (a) Intensity *vs.* time graph corresponding to NO_2 absorbance at 500 nm at various concentrations of 500 ppm, 1000 ppm, 2500 ppm and 5000 ppm recorded twice. (b) Standard deviation graph illustrating the intensity changes of the wavelengths in the range of 400–700 nm for all concentrations.

overlaps with the NO_2 absorbance, it is quite inappropriate to monitor the centroid/peak position. It should be noted that the former approach has been carried out by our group in order to de-convolute the response of CO gas at 800 °C since the absorbance of CO (NIR region) does not overlap with the plasmon peak (visible region).[25] Hence in the present work, intensity as a function of time has been monitored in the wavelength range of 400–700 nm as shown in Fig. 7 to examine for differences in the intensity changes when only NO_2 was present within the monitoring cell.

In order to quantify the absorbance intensity changes with only NO_2, two iterations have been performed at 800 °C for all gas concentrations (500 ppm, 1000 ppm, 2500 ppm, and 5000 ppm) as shown in Fig. 7(a). It has been observed that the absorbance intensity of NO_2 has increased upon increasing the concentrations for both iterations. The change in intensity value has been plotted with standard deviations for the wavelength range of 400–700 nm as in Fig. 7(b). The wavelengths have been limited to 700 nm since the absorbance beyond this range was negligible (approaching baseline noise levels) for all concentrations and temperatures. If the response of the AGOs to NO_2 at 800 °C goes beyond the values as in Fig. 4 we then can arrive at a conclusion that the composites have a distinct response to NO_2.

3.4.2 Gas sensing tests on AGOs. Post the tests at multiple temperatures to establish the changes in optical absorbance with only NO_2, the AGOs were all tested for their responses by examining the changes in absorbance intensities as a function of temperature and concentration. From the graphs as in Fig. 8 for the representative AIGO, it is conclusive that the change in the intensity in the presence of the sample is beyond that when only NO_2 is present, as shown in Fig. 9d (and in the ESI,† Fig. S16 and S17).

All AGOs were examined by this method to arrive at the optimal configuration, and the corresponding graphs are given in Fig. S9–S15 (ESI†).

After analysis of the sensing exposure data, calibration curves showing the changes in the intensity of all samples were determined and are shown in Fig. 9. The assessment has been carried out only in the plasmonic region from 500 to 650 nm due to the presence of the plasmonic peak of all AGOs in this region. Plausible mechanisms that occur upon gas exposure between the samples and NO_2 are included in Section 3.4.3. It is noteworthy that across the plasmonic region, AIGO exhibits a maximum intensity change compared to other AGOs, although all the other composites were responsive to NO_2 at 800 °C. A plausible explanation for the maximum response of AIGO may stem from the combination of a more uniform dispersion of AuNPs within the composite (as can be qualitatively confirmed from the TEM images of this sample), comparatively minimal alterations in the volume expansion of AuNPs post-high temperature exposure (as confirmed by the least changes to the plasmon peak shown in Fig. 3), a higher particle density on the substrate that has enhanced the sensitivity, and a higher consistency in crystallinity as observed in XRD data following high temperature exposure,[28] apart from enhancements to sensitivity resulting possibly from a higher tri-phase boundary effect, a well-established governing authority in catalytic reactions.[43–45]

As noted before, the modifications to morphologies are difficult to directly visualize[28,30] as the composites are coated onto quartz substrates measuring 10 × 10 × 1 mm, posing challenges during TEM sample preparation in terms of an arduous crimping process to reduce the substrate size to 3 × 3 mm (for imaging), often resulting in substrate breakage and sample loss.

3.4.3 Mechanisms governing the plasmonic response of AGOs to NO_2. A plausible gas sensing mechanism to detect NO_2 is presented in Fig. 10. At 800 °C reactive oxygen species (such as O^- and O^{2-}) are chemisorbed on surface sites, followed by migration into vacancy sites in the bulk.[44,46] The role of the plasmonic nanoparticle and the metal oxide is better explained as follows: the metal oxide acts as a source of oxygen vacancy sites allowing migration into and out of these sites by oxygen as it reacts with NO_2. The metal oxide also stabilizes the AuNPs at high temperatures against a change in morphology. The AuNPs, on the other hand, act as reaction mediators, for example, by enabling charge transfer through the tri-phase boundary, apart from enhancing the charge transfer by the plasmonic effect that

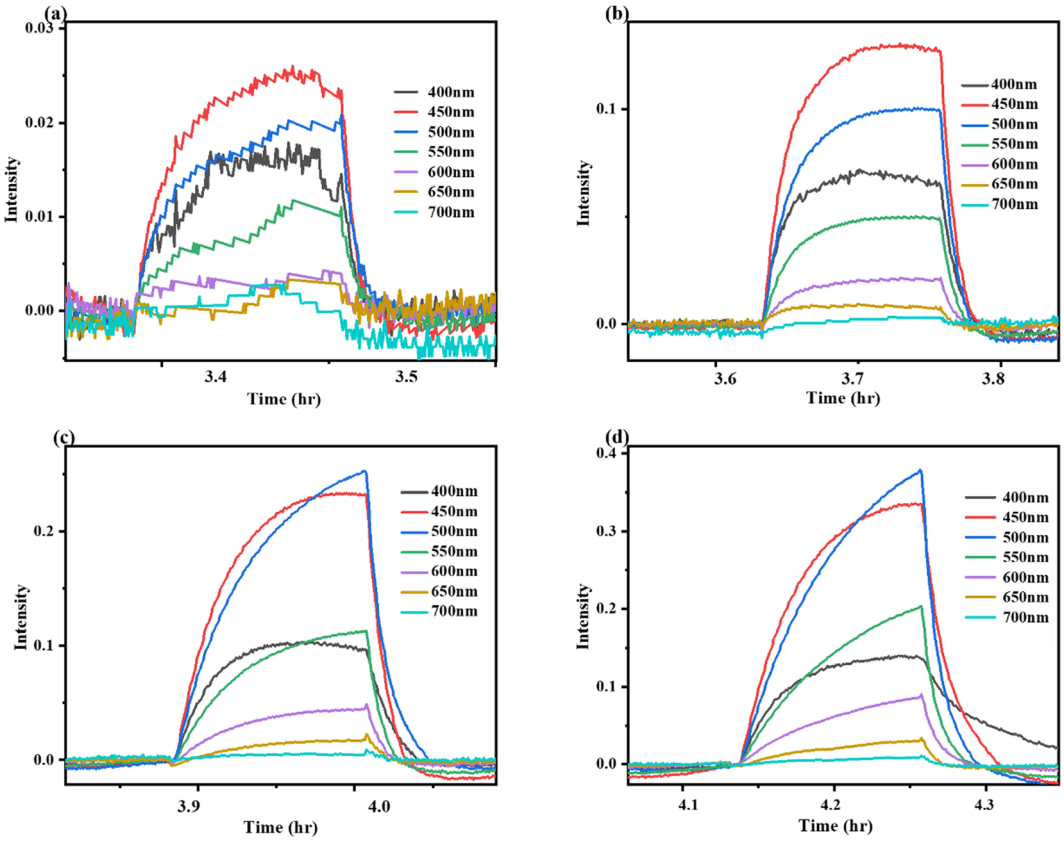

Fig. 8 Sensing responses of AIGO towards NO_2 at 800 °C at concentrations of (a) 500 ppm, (b) 1000 ppm, (c) 2500 ppm and (d) 5000 ppm as a function of wavelength.

stems primarily from the enhanced local electromagnetic fields of the plasmons. Adsorption results in a decrease in plasmon frequency due to a decrease in free electron density or an increase in frequency due to a decrease in polarizability of the matrix (depending on the specific interactions of the adsorbing oxygen with Au NPs or Ga_2O_3).[47] Desorption results in the opposite. The equation of plasmon frequency is given by

$$\omega_p = \sqrt{\frac{ne^2}{m \cdot \varepsilon_0}} \quad (1)$$

where n is the electron density, e is the charge of the electron, m is the electron effective mass in the material, and ε_0, the permittivity of vacuum, can better serve for envisaging these changes.[48]

The reaction pathways for oxygen adsorption can be written as:

$$O_{2(g)} + Vo_{(s)} + Ga_{(s)}^{3+} \rightarrow O_{2(ads)} + Ga_{(s)}^{4+} \quad (2)$$

(or)

$$O_{2(g)} + Vo_{(s)} + Au_{(s)} \rightarrow O_{2(ads)} + Au_{(s)}^{2+} \quad (3)$$

$$O_{2(ads)} + V_{O(b)} \rightarrow O_{2(b)} \quad (4)$$

where subscripts g, s, b, and ads denote gas phase, surface, bulk and adsorption, respectively. Oxygen vacancies are hence filled by the adsorbing oxygen during the preliminary exposure to air at 800 °C.[23,49]

Upon NO_2 exposure, the gas molecules extract chemisorbed oxygen ions from the vacancies, which ultimately decreases the free electron density and plasmon frequency and/or increases the polarizability of the matrix, and the wavelength shifts toward the red compared to the baseline spectrum. The reaction pathways upon NO_2 exposure can be written as follows:[50]

$$NO_2 + 2O_{(s)}^- \rightarrow NO_2^-{}_{(ads)} + O_2 + e^- \quad (5)$$

$$NO_2^-{}_{(ads)} + O_2 + e^- \rightarrow NO + 1/2O_2 + 2O^- \quad (6)$$

As shown in Fig. 10, the intensity of the peaks changed at all concentrations, corroborating the mechanisms between AGO and NO_2. With this understanding, studies of temperature driven sensing responses of the best responding AIGO sample were performed to reveal the mechanistic phenomenon underlying sensing reactions.

3.4.4 Temperature-driven gas kinetics of AIGO towards NO_2. We have carried out a temperature-dependent (400 °C, 600 °C, and 800 °C) study as a function of wavelength for various concentrations 500 ppm, 1000 ppm, 2500 ppm, and 5000 ppm as shown in Fig. 11. Since this report aims to develop materials that can perform sustained detection of NO_2 for high temperature emissions (>300 °C), such as from boilers (500–700 °C), gas turbines (>800 °C), steam turbines (400–600 °C), glass-making industries (400–700 °C), *etc.*, wherein typical concentration ranges that are monitored are 250–650 ppm,

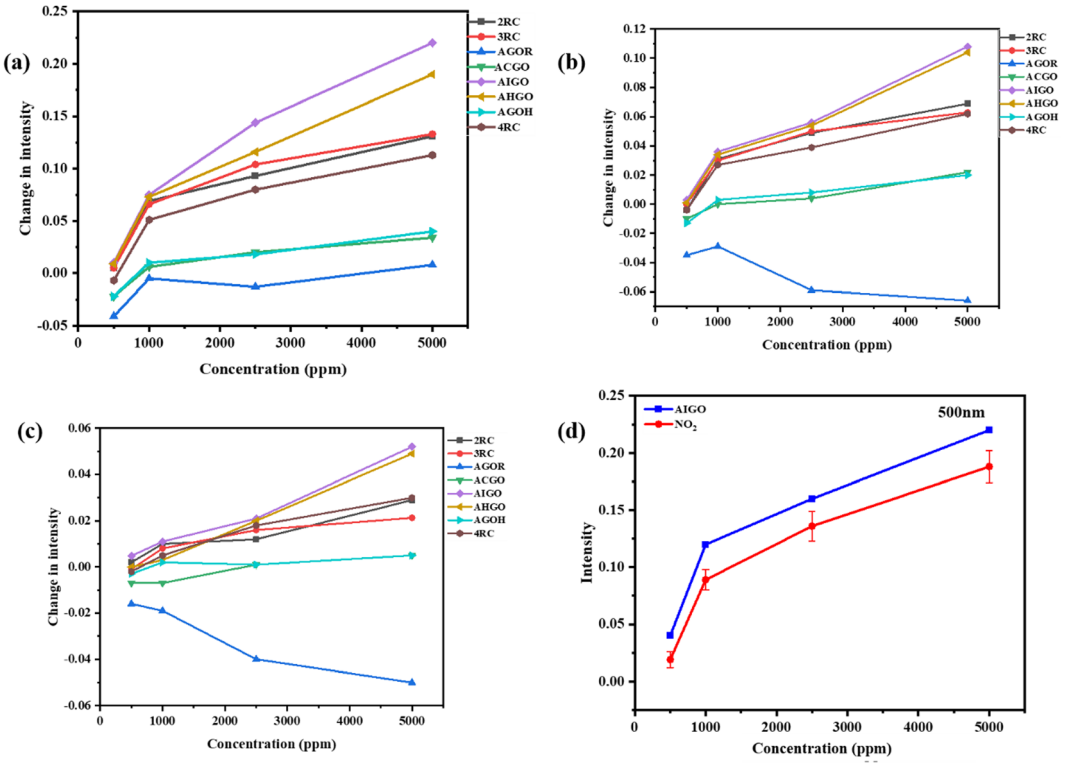

Fig. 9 Wavelength investigation of AGOs in the plasmonic region: (a) 500 nm, (b) 550 nm, and (c) 600 nm at concentrations of 500 ppm, 1000 ppm, 2500 ppm, and 5000 ppm and (d) the comparison graph of the change in the absorbance intensity of NO_2 without the sample and with AIGO at 500 nm.

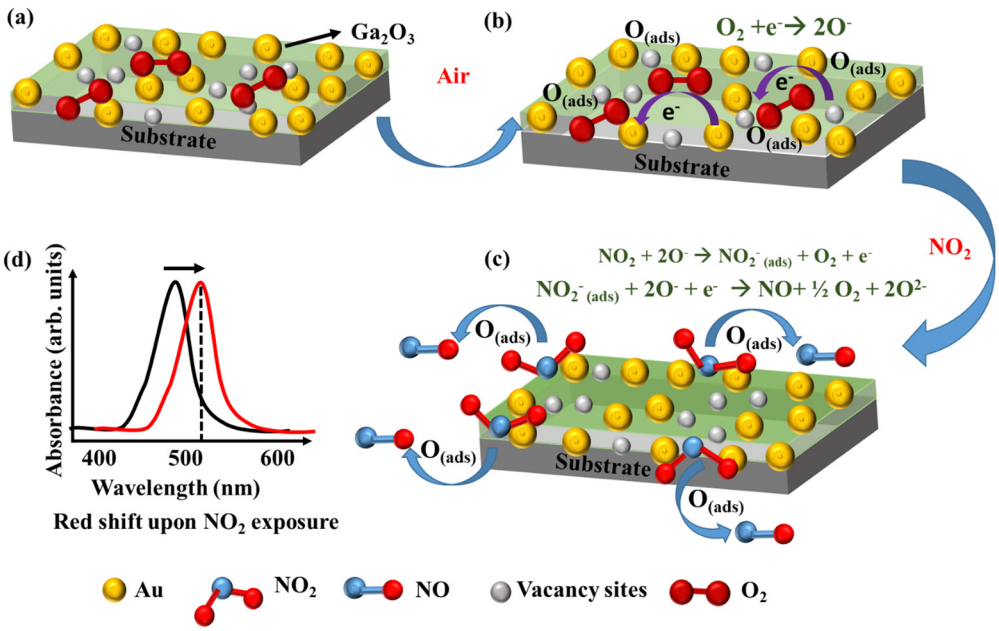

Fig. 10 Gas sensing mechanism of AGOs towards NO_2 at 800 °C: (a) AGO on a quartz substrate. (b) AGO exposed to air at 800 °C. (c) AGOs exposed to NO_2 in air background. (d) Shift towards the longer wavelength/redshift upon gas exposure.

2–20 ppm, 141–929 ppm, and 640 ppm respectively, the investigated temperature range for gas kinetics was chosen from 400 to 800 °C.[51,52]

At higher temperatures, vacancy mediated reactions tend to increase due to higher ad/desorption reactions. Hence, the response to NO_2 was envisaged to increase, but in contrast,

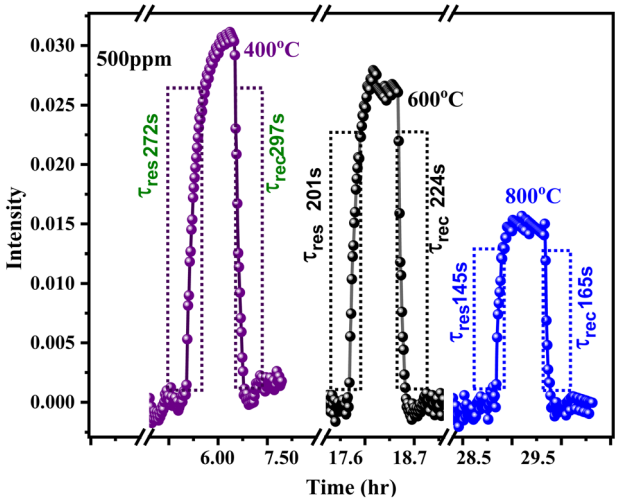

Fig. 11 Temperature-dependent sensing response of AlGO towards NO_2 at 500 ppm at different temperatures: 400 °C, 600 °C and 800 °C.

the response linearly decreased, as revealed in Fig. 11. A similar trend has been reported by Rogers *et al.*, wherein the authors have reported this change due to increased mass transport kinetics at high temperatures, *i.e.* when the gas molecules are heated, the volume of the gas increases according to the ideal gas equation PV = *n*RT.[53,54] Hence the number of NO_2 molecules/population decreases with the increase in temperature in the testing chamber, possibly causing reduced sensitivity (Fig. 12).

The response and recovery times have decreased as well with an increase in temperature. To explain these changes in time, it is necessary to take into consideration the temperature-dependent adsorption/desorption processes. Langmuir's theory predicts the adsorption equilibrium through the equation[55]

$$N = \frac{N^* P \chi_s}{\nu\sqrt{2\pi MkT}} e^{(q/kT)} \quad (7)$$

where N is the total number of adsorbed molecules, N^* is the maximum number of molecules that can be adsorbed on the surface, P is the pressure, M is the mass of the adsorbed molecules, s is the effective surface area, q is the activation energy required for the reaction, k is the Boltzmann constant and T is the absolute temperature. From this equation, it can be observed that the number of adsorbed molecules (N) diminishes with an increase in the temperature, and hence the observed decrease in sensitivity could be envisaged when the sensing material is exposed to a higher temperature.[56] The decrease in the sensing response with an increase in temperature could be attributed to several other reasons as well, such as (i) at high temperatures, gas molecules possess greater kinetic energy, which could disrupt the interactions between the gas molecules and the sensing material resulting in a reduced

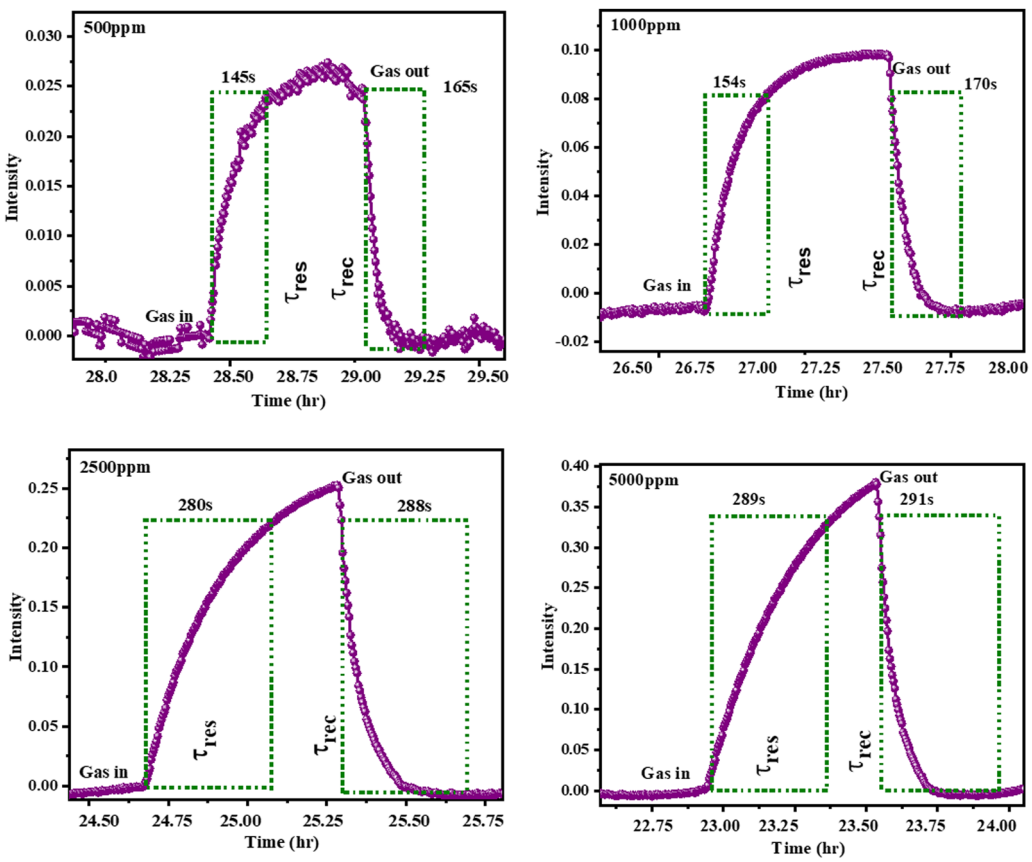

Fig. 12 Response and recovery time of the AlGO composite at 800 °C for various concentrations.

response[57] and (ii) elevated temperatures can cause structural changes or phase transitions in the sensing material affecting the morphology and chemical composition.[57] These changes can diminish the material's ability to interact with the gas molecules. Our group has carried out an exhaustive analysis of the composites with respect to changes in structural and phase transitions of AuNP–Ga_2O_3 composites and confirmed that no detrimental phase transitions (such as the occurrence of secondary phases/oxidation, *etc.*), chemical composition variation, and varying degrees of changes in the morphology of AuNPs can be observed.[28,30] Thus the discussion on the driving forces behind the reaction kinetics can be focussed largely on the discussion regarding the kinetic changes to gas–sample interactions at elevated temperatures. Hence, it is conclusive that at higher temperatures gas kinetics dictate a reduced number of adsorbed molecules and hence a reduced interaction, insofar as the composites investigated herein are contemplated. The promise of long-term sensing stability can be expected from these compositions (and are currently underway), as we have previously demonstrated[23–25] that such composites of metal nanoparticles and metal oxides can be remarkably stable against temperature induced permanent changes to their optical and catalytic properties for multiple hundreds of hours. The challenge of selectivity, omnipresent in any material developed for sensing gas mixtures, can also in part be addressed by morphological control, as we have demonstrated that parameters such as the particle size can be used to enhance or suppress the gas sensing response between the same family (reducing) of gases (CO *vs.* H_2).

4. Conclusions and outlook

To summarize, this report details a suitable plasmonic material incorporated metal oxide composite for high temperature detection of NO_2, realized through an unsophisticated solution based approach for the first time. AGCs synthesized using a straightforward *in situ* hydrothermal approach can thus be used as potential candidates for real time monitoring of emissions of such gases in harsh environments, such as boiler plants, steam and gas turbines, glass making industries, food processing units, *etc.* The Au NPs presented in this study, when integrated with Ga_2O_3, exhibited hitherto unobserved morphological stability against temperature. Previous reports have employed the fabrication of such material combinations through physical vapor deposition, chemical vapor deposition, lithography, *etc.*, involving expensive equipment and intensive power. We have realized the composites through relatively much simpler processes and proposed the hydrothermal approach for composite preparation as it allows repeatable results over size and morphology distributions, enabling the formation of uniform structures.

A unique finding in this study is that the use of discrete wavelength-based investigations can significantly enable the use of plasmonic composites that have overlapping absorption with the analyte to be sensed. In particular, the confirmation of the sensitivity of the absorbance changes of the analyte to those when both the sample and analyte are present can be differentiated through this approach. Hitherto unusable Au and Ag based composites can hence be explored for the presence of a distinct response to relevant analytes. The necessity of careful analysis (to confirm a response magnitude above the average response with only the analyte) and repeated measurements of the sensing response (to ascertain the increased sensitivity of the sample compared to just the analyte) must be underscored, however. To the best of our knowledge, a plasmonically active composite has not been reported for NO_2 sensing at a temperature of 800 °C to date. The approach of investigating individual wavelengths is the crucial aspect here, as contemplating changes in the SPR peak in its entirety will lead to errors in calculating the response due to the overlap in absorbance.

To suggest a few directions for furthering this work, integrating AuNPs of smaller particle sizes with Ga_2O_3 (for a higher rate of dissociation of the analyte due to a higher surface-to-volume ratio), encapsulating the plasmonic structures within the matrix in a core–shell architecture (with the matrix being the shell, possibly providing enhanced stability and protection for the NPs), optimizing the loading of Au NPs in the AGCs thereby enhancing, for example, the spillover effect leading to improved charge transfer, and fabricating sensor arrays made of different metal oxides that can have cross-sensitivity to multiple gases will all influence the choice of the analyte gas, the operating range, and the sensor performance metrics. For example, developing a sensing material with the plasmon band peaking beyond 600 nm can be a simpler option for sensing gases like NO_2 that tend to absorb naturally in the visible region (the tendency for spheroidization at high temperatures notwithstanding) albeit presumably not for the temperatures reported here. Hence, fabrication of morphologies such as Au NRs, nanoflowers, and mixed polygons must be done keeping this in mind with steps such as functionalizing the NPs with ligands that can anchor the metal oxide for better morphological stability. These structures can still be realized when one chooses to work with simple solution-based material development.

Data availability

The authors confirm that all the data generated in this manuscript have been made available in the manuscript and/or the ESI.†

Conflicts of interest

There are no conflicts to declare.

Acknowledgements

The authors sincerely thank the Aeronautical Research & Development Board, Govt of India (sanction code: DGTM/TM/ARDB/GIA/18-19/0296, Project No: 2031895) for supporting this study.

References

1 S. Cheval, C. M. Adamescu, T. Georgiadis, M. Herrnegger, A. Piticar and D. R. Legates, *Int. J. Environ. Res. Public Health*, 2020, **17**, 4140.
2 C. E. Baukal and P. B. Eleazer, Quantifying NOx for industrial combustion processes, *J. Air Waste Manage. Assoc.*, 1998, **48**, 52–58.
3 P. Saxena and S. Sonwani, *Criteria Air Pollutants and their Impact on Environmental Health*, Springer Nature, Springer Singapore, 2019, 1.
4 K. I. Jolic, C. R. Nagarajah and W. Thompson, Nom-contact, optically based measurement of surface roughness of ceramics, *Meas. Sci. Technol.*, 1994, **5**, 671.
5 Y. K. Zhu, G. Y. Tian, R. S. Lu and H. Zhang, A review of optical NDT technologies, *Sensors*, 2011, **11**, 7773–7798.
6 S. B. Khan, M. T. S. Chani, K. S. Karimov, A. M. Asiri, M. Bashir and R. Tariq, *Talanta*, 2014, **120**, 443–449.
7 M. P. Da Cunha, T. Moonlight, R. Lad, D. Frankel and G. Bernhardt, *Proc. IEEE Sens.*, 2008, 205–208.
8 S. Sarma, S. Singh and A. Garg, *Measurement*, 2021, **172**, 108876.
9 L. Keerthana, M. Ahmad Dar and G. Dharmalingam, *Chem. – Asian J.*, 2021, **16**, 3558–3584.
10 H. Jin-Yong, H. Lei, H.-Y. Zhang, X.-X. Xue, X.-P. Wang, C.-H. Wang and Y. Zhang, *Rare Met.*, 2024, **12**(43), 6500–6515.
11 W. Ting-Ting, B.-S. Xing, C.-Y. Guo, J.-Y. Hao, Y. Wang, L.-H. Huo, X.-L. Cheng and Y.-M. Xu, *Rare Metals*, 2023, **12**(42), 3897–3913.
12 Z. Yue, M.-Y. Wang, X.-G. San, Y.-B. Shen, G.-S. Wang, L. Zhang and D. Meng, *Rare Met.*, 2024, **1**(43), 267–279.
13 H. Jinyong, X. Liu, J. Zhang, X. Gu and Y. Zhang, *Sens. Actuators, B*, 2023, **382**, 133505.
14 H. Jinyong, X. Wang, H. Lei, M. Luo and Y. Zhang, *Sens. Actuators, B*, 2024, **407**, 135422.
15 W. Ding, D. Liu, J. Liu and J. Zhang, *Chin. J. Chem.*, 2020, **38**, 1832–1846.
16 L. Keerthana, M. Ahmad Dar and G. Dharmalingam, *Chem. Asian J.*, 2021, **16**, 3558–3584.
17 C. H. Liang, G. W. Meng, G. Z. Wang, Y. W. Wang, L. D. Zhang and S. Y. Zhang, *Appl. Phys. Lett.*, 2001, **001**(78), 3202–3204.
18 Z. Liu, T. Yamazaki, Y. Shen, T. Kikuta, N. Nakatani and Y. Li, *Sens. Actuators, B*, 2008, **129**, 666–670.
19 F. Safieddine, F. E. H. Hassan and M. Kazan, *J. Solid State Chem.*, 2022, **312**, 123272.
20 B. Zhao, X. Li, L. Yang, F. Wang, J. Li, W. Xia, W. Li, L. Zhou and C. Zhao, *Photochem. Photobiol.*, 2015, **91**, 42–47.
21 G. Dharmalingam and M. A. Carpenter, *Sens. Actuators, B*, 2017, **251**, 1104–1111.
22 N. Karker, G. Dharmalingam and M. A. Carpenter, *ACS Nano*, 2014, **8**, 10953–10962.
23 G. Dharmalingam, N. A. Joy, B. Grisafe and M. A. Carpenter, *Beilstein J. Nanotechnol.*, 2012, **3**(81), 712–721.
24 L. Keerthana, A. R. Indhu and G. Dharmalingam, *J. Mater. Res.*, 2023, **38**, 497–506.
25 K. Narayanan and D. Gnanaprakash, *J. Clust. Sci.*, 2022, **33**, 227–240.
26 L. Keerthana, A. R. Indhu and G. Dharmalingam, *App. Nano.*, 2022, **12**, 2857–2871.
27 K. Narayanan and G. Dharmalingam, *J. Phy. Chem. Sol.*, 2024, **185**, 111800.
28 J. R. Lakowicz, *Plasmonics*, 2006, **1**, 5–33.
29 J. Kennedy, M. Soos, A. Vaccaro and M. Morbidelli, *Chem. Eng. Process.*, 2006, **45**(10), 936–943.
30 L. Keerthana and G. Dharmalingam, *Phys. Chem. Chem. Phys.*, 2024, 15018–15031.
31 S. Shrestha, B. Wang and P. Dutta, *Adv. Colloid Interface Sci.*, 2020, **279**, 102162.
32 L. Fu, Y. Liu, P. Hu, K. Xiao, G. Yu and D. Zhu, *Chem. Mater.*, 2003, **15**, 4287–4291.
33 X. Wang, J. Wu, Y. Zhang, Y. Sun, K. Ma, Y. Xie, W. Zheng, Z. Tian, Z. Kang and Y. Zhang, *Adv. Mater.*, 2023, **35**, 2206576.
34 S. Park, M. Kim, Y. Lim, D. H. Oh, J. Ahn, C. Park, S. Woo, W. C. Jung, J. Kim and I. D. Kim, *Adv. Mater.*, 2024, 2313731.
35 H. A. Bent, Dimers of Nitrogen Dioxide. II. Structure and Bonding, *Inorg. Chem.*, 1963, **2**, 747–752.
36 A. Amoruso, L. Crescentini, G. Fiocco and M. Volpe, *J. Geophys. Res.*, 1993, **98**, 816–857.
37 J. A. Davidson, C. A. Cantrell, A. H. McDaniel, R. E. Shetter, S. Madronich and J. G. Calvert, *J. Geophys. Res.*, 1988, **93**, 7105–7112.
38 I. Zyrichidou, M. E. Koukouli, D. Balis, K. Markakis, A. Poupkou, E. Katragkou, I. Kioutsioukis, D. Melas, K. F. Boersma and M. van Roozendael, *Atmos. Environ.*, 2015, **101**, 82–93.
39 M. H. Harwood and R. L. Jones, *J. Geophys. Res.*, 1994, **99**, 22955–22964.
40 M. F. Merienne, A. Jenouvrier and B. Coquart, *J. Atmos. Chem.*, 1995, **20**, 281–297.
41 A. B. Dahlin, J. O. Tegenfeldt and F. Höök, Improving the instrumental resolution of sensors based on localized surface plasmon resonance, *Anal. Chem.*, 2006, **78**, 4416–4423.
42 R. You, X. Hao, H. Yu, B. Wang, G. Lu, F. Liu and T. Cui, *Sens. Actuators, B*, 2018, **263**, 445–451.
43 S. Lv, Y. Zhang, L. Jiang, L. Zhao, J. Wang, F. Liu, C. Wang, X. Yan, P. Sun, L. Wang and G. Lu, *Sens. Actuators, B*, 2022, **354**, 131219.
44 X. Liang, S. Yang, J. Li, H. Zhang, Q. Diao, W. Zhao and G. Lu, *Sens. Actuators, B*, 2011, **158**, 1–8.
45 M. Al-Hashem, S. Akbar and P. Morris, *Sens. Actuators, B*, 2019, **301**, 126845.
46 P. K. Jain and M. A. El-Sayed, *Chem. Phys. Lett.*, 2010, **487**, 153–164.
47 C. David and F. J. García De Abajo, *ACS Nano*, 2014, **8**, 9558–9566.
48 G. Dharmalingam, N. A. Joy, B. Grisafe and M. A. Carpenter, *Beilstein J. Nanotechnol.*, 2012, **3**, 712–721.
49 G. Dharmalingam and M. A. Carpenter, Proceedings Volume Sensors for Extreme Harsh Environments II, SPIE, 2015, p. 949101, DOI: **10.1117/12.2199541**.
50 I. Zyrichidou, M. E. Koukouli, D. Balis, K. Markakis, A. Poupkou, E. Katragkou, I. Kioutsioukis, D. Melas, K. F. Boersma and M. van Roozendael, *Atmos. Environ.*, 2015, **101**, 82–93.

51 R. J. van der A, H. J. Eskes, K. F. Boersma, T. P. C. van Noije, M. Van Roozendael, I. De Smedt, D. H. M. U. Peters and E. W. Meijer, *J. Geo. Res. Atm*, 2008, **113**, D04302.
52 N. A. Joy, P. H. Rogers, M. I. Nandasiri, S. Thevuthasan and M. A. Carpenter, *Anal. Chem.*, 2012, **84**, 10437–10444.
53 N. A. Joy, M. I. Nandasiri, P. H. Rogers, W. Jiang, T. Varga, S. V. N. T. Kuchibhatla, S. Thevuthasan and M. A. Carpenter, *Anal. Chem.*, 2012, **84**, 5025–5034.
54 H. Swenson and N. P. Stadie, *Langmuir*, 2019, **35**(16), 5409–5426.
55 Q. Chen, Y. Tian, P. Li, C. Yan, Y. Pang, L. Zheng, H. Deng, W. Zhou and X. Meng, *J. Chem.*, 2017, **1**, 1496463.
56 Patiha, E. Heraldy, Y. Hidayat and M. Firdaus, *IOP Conf. Ser. Mater. Sci. Eng.*, 2016, 012067.
57 D. A. H. Hanaor and C. C. Sorrell, *J. Mater. Sci.*, 2011, **46**, 855–874.